



UNDRAINED STABILITY OF A SQUARE TUNNEL IN A SOIL WHOSE STRENGTH INCREASES LINEARLY WITH DEPTH

S W Sloan and A Assadi
Department of Civil Engineering and Surveying
University of Newcastle
NSW 2308

ABSTRACT

This paper examines the undrained stability of a shallow square tunnel in a soil whose strength increases linearly with depth. Rigorous bounds on the loads needed to resist collapse are derived using two numerical techniques which are based on finite element formulations of the classical limit theorems. Both of the numerical procedures assume a linearized perfectly plastic soil model and require the solution of large sparse linear programming problems. For the range of tunnel geometries considered, the numerical results bracket the exact collapse loads closely. The solutions are presented in the form of stability charts which can be used by practising engineers for the purposes of design.

INTRODUCTION

This paper considers the stability of a long square tunnel in a soil whose shear strength increases linearly with depth. Loading is assumed to take place under undrained conditions in a state of plane strain. The tunnel, shown in Figure 1, is of dimension B and rests at a depth H below the ground surface. Collapse, which is triggered by the action of gravity and the surcharge σ_s , is resisted by the internal tunnel pressure σ_t and the undrained shear strength of the soil. The latter is assumed to vary according to

$$c_u(z) = c_{u0} + \rho z \quad (1)$$

where c_{u0} is the undrained shear strength at the ground surface and $\rho = dc_u/dz$ is the rate of change of shear strength with depth. The overall stability of the tunnel may be described conveniently by two load parameters, $(\sigma_s - \sigma_t)/c_{u0}$ and $\gamma B/c_{u0}$, which are functions of $\rho B/c_{u0}$ and H/B . In most cases $\gamma B/c_{u0}$, $\rho B/c_{u0}$ and H/B are known and

it necessary to be able to ascertain the value of $(\sigma_s - \sigma_t)/c_{u0}$ at incipient collapse. Although this problem occurs frequently in civil engineering works, it does not appear to have been widely studied.

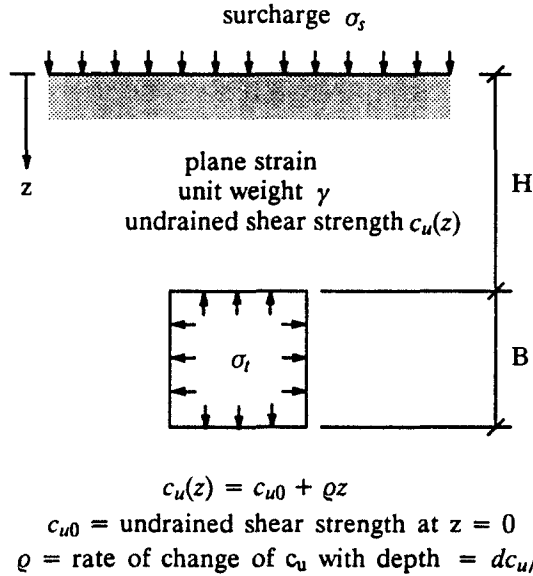


Figure 1: Square tunnel in soil whose strength increases linearly with depth

For a range of shallow tunnel geometries, this paper describes the application of two numerical techniques to yield sharp bounds on the load parameter $(\sigma_s - \sigma_t)/c_{u0}$. The numerical schemes are based on a finite element formulation of the plastic limit theorems and lead to large linear programming problems. The kinematically admissible velocity field obtained by solving the upper bound optimization problem can be used to find an unsafe estimate of the collapse pressures. The solution to the lower bound optimization problem, on the other hand, defines a statically admissible stress field and thus yields a safe estimate of the collapse pressures. For the range of tunnel geometries considered in this paper, the numerical solutions typically bound the exact stability number to within 15 percent or better.

A detailed description of the lower bound and upper bound formulations, including explicit coding details, may be found in Sloan [1,2]. This material will not be repeated here but a condensed outline of each technique will be given to illustrate the overall approach. Although elegant and powerful, the numerical schemes have not been used widely in soil mechanics applications. To appreciate the significance of the results, some understanding of the requirements and implications of the classical bound theorems is necessary.

NUMERICAL FORMULATION OF THE LOWER BOUND THEOREM

The lower bound theorem assumes a rigid plastic soil model and states that any statically admissible stress field, which satisfies equilibrium, the stress boundary conditions and the yield criterion, will provide a rigorous lower bound on the true collapse load. Although this theorem has been widely used in geotechnical design, it is often very difficult to apply to practical problems involving complex loadings or complicated geometries.

The use of finite elements and linear programming to compute rigorous lower bounds for soil mechanics problems appears to have been first proposed by Lysmer [3]. This formulation employed 3-noded triangular elements to model the stress field and illustrated the advantages of computing lower bounds numerically. Although Lysmer's procedure was potentially very powerful, its utility was initially limited by the slowness of the algorithms that were available for solving large linear programming problems. In recent years, major advances have been made in this area and the numerical stability of the formulation has also been improved remarkably. Since a typical lower bound optimization problem may involve several thousand unknowns, and an even larger number of constraints, it is essential to fully exploit any of its special features. In particular, the extreme sparsity of the overall constraint matrix should be taken into account to reduce the computation time and storage requirements. Detailed discussions of various lower bound approaches may be found in Anderheggen and Knopfel [4], Pastor [5] and Bottero *et al.* [6]. More recently, Sloan [1,2] has introduced a formulation which uses a newly developed active set algorithm and permits very large problems to be solved efficiently on a workstation or microcomputer. Advantages of the finite element method of computing lower bounds are numerous and include the ability to deal with complex loadings, complicated geometries and inhomogeneous soils.

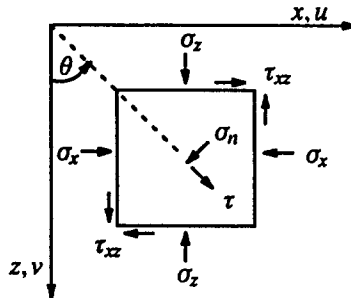


Figure 2: Sign convention for velocities and stresses

The sign conventions for the stresses, with compression taken as positive, are as shown in Figure 2. Three types of elements are employed, as depicted in Figure 3, and each of these permit the stresses to vary linearly according to

$$\sigma_x = \sum_{i=1}^{i=3} N_i \sigma_{xi} \quad ; \quad \sigma_z = \sum_{i=1}^{i=3} N_i \sigma_{zi} \quad ; \quad \tau_{xz} = \sum_{i=1}^{i=3} N_i \tau_{xzi} \quad (2)$$

where N_i are linear shape functions and $\sigma_{xi}, \sigma_{zi}, \tau_{xzi}$ are nodal stresses. Note that the rectangular and triangular extension elements, which enable a statically admissible stress field to be obtained for a semi-infinite domain, are based on the same linear expansion as the 3-noded triangle.

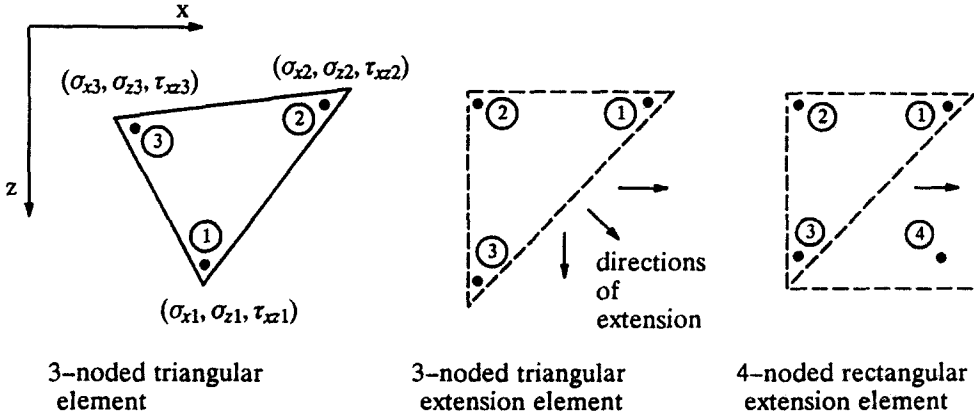


Figure 3: Elements for lower bound analysis

A simple illustrative lower bound mesh for a square tunnel is shown in Figure 4. Unlike the more familiar types of elements used in the displacement finite element method, each node is unique to a single element and several nodes may share the same coordinates. To broaden the range of stress fields that are available to a particular mesh, statically admissible stress discontinuities are permitted at all edges that are shared by adjacent elements, including those edges that are shared by adjacent extension elements. A rigorous lower bound on the exact collapse load is ensured by insisting that the stresses obey equilibrium and satisfy both the stress boundary conditions and the yield criterion. Each of these requirements imposes a separate set of constraints on the nodal stresses.

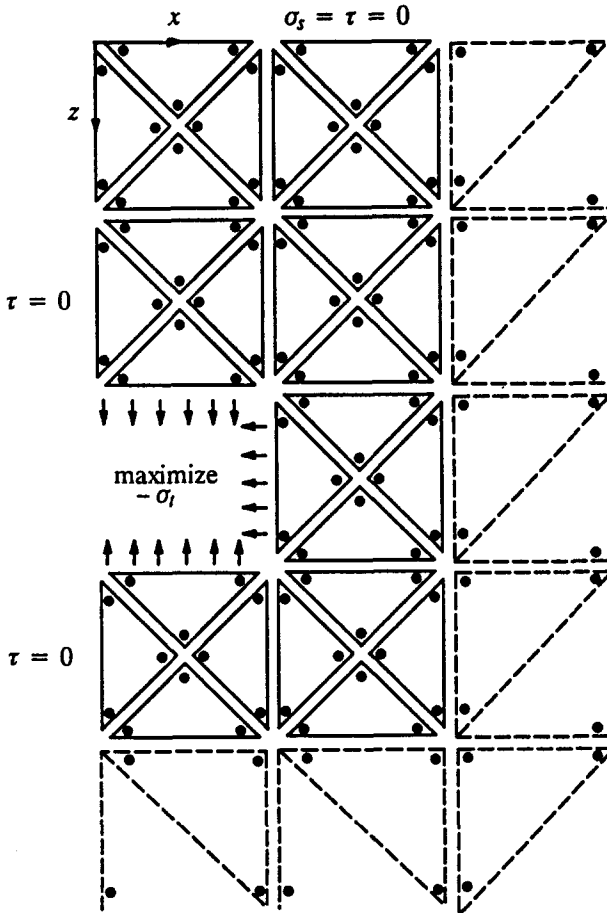
Noting the sign convention of Figure 2, the equilibrium conditions for plane strain are

$$\frac{\partial \sigma_x}{\partial x} + \frac{\partial \tau_{xz}}{\partial z} = 0 \quad ; \quad \frac{\partial \sigma_z}{\partial z} + \frac{\partial \tau_{xz}}{\partial x} = \gamma \quad (3)$$

Substituting equations (2) in (3), we see that the nodal stresses for each element are subject to two equilibrium constraints of the form

$$\mathbf{a}_1 \mathbf{x} = \mathbf{b}_1 \quad (4)$$

where \mathbf{a}_1 is a function of the nodal coordinates, $\mathbf{x} = \{\sigma_{x1}, \sigma_{z1}, \tau_{xz1}, \dots, \sigma_{x3}, \sigma_{z3}, \tau_{xz3}\}^T$ and $\mathbf{b}_1 = \{0, \gamma\}^T$.



28 triangular elements
 6 rectangular extension elements
 1 triangular extension element
 47 discontinuities

Figure 4: Illustrative lower bound mesh for square tunnel

For each rectangular extension element, three additional equalities are necessary to extend the linear stress distribution to the fourth node. These equalities are

$$\sigma_{x4} = \sigma_{x1} + \sigma_{x3} - \sigma_{x2} \quad ; \quad \sigma_{z4} = \sigma_{z1} + \sigma_{z3} - \sigma_{z2} \quad ; \quad \tau_{xz4} = \tau_{xz1} + \tau_{xz3} - \tau_{xz2}$$

and may be written as

$$\mathbf{a}_2 \mathbf{x} = \mathbf{b}_2 \tag{5}$$

where \mathbf{a}_2 is a matrix of constants, $\mathbf{x} = \{\sigma_{x1}, \sigma_{z1}, \tau_{xz1}, \dots, \sigma_{x4}, \sigma_{z4}, \tau_{xz4}\}^T$ and $\mathbf{b}_2 = \{0, 0, 0\}^T$. The fourth node of the rectangular extension element is essentially a dummy node but is necessary to permit semi-infinite stress discontinuities between adjacent extension elements.

A stress discontinuity is statically admissible if the shear and normal stresses acting on the discontinuity plane are continuous (only the tangential stress may jump). Since the stresses are assumed to vary linearly, this condition is met by forcing all pairs of nodes on opposite sides of the discontinuity to have equal shear and normal stresses. A typical discontinuity is defined by two nodal pairs, where the nodes in each pair have identical coordinates, and gives rise to four equality constraints. Using the well known stress transformation equations, which relate the stresses on an arbitrary plane to the cartesian stresses, the equilibrium conditions for each discontinuity may be written as

$$\mathbf{a}_3 \mathbf{x} = \mathbf{b}_3 \quad (6)$$

where \mathbf{a}_3 depends on the orientation of the discontinuity, $\mathbf{x} = \{\sigma_{x1}, \sigma_{z1}, \tau_{xz1}, \dots, \sigma_{x4}, \sigma_{z4}, \tau_{xz4}\}^T$ and $\mathbf{b}_3 = \{0, 0, 0, 0\}^T$.

To enforce prescribed boundary conditions, it is necessary to impose additional equality constraints on the nodal stresses. If the normal and shear stresses at the ends of a boundary segment are specified to be (σ_{n1}, τ_1) and (σ_{n2}, τ_2) , then substitution into the stress transformation equations leads to four equalities of the general form

$$\mathbf{a}_4 \mathbf{x} = \mathbf{b}_4 \quad (7)$$

where \mathbf{a}_4 depends on the orientation of the edge, $\mathbf{x} = \{\sigma_{x1}, \sigma_{z1}, \tau_{xz1}, \sigma_{x2}, \sigma_{z2}, \tau_{xz2}\}^T$ and $\mathbf{b}_4 = \{\sigma_{n1}, \tau_1, \sigma_{n2}, \tau_2\}^T$. When applied to a semi-infinite edge of an extension element, equation (7) ensures that the stress boundary conditions are satisfied everywhere along the edge.

A key feature of the lower bound formulation is the use of a linearized yield criterion. This is necessary to avoid nonlinear constraints. Under conditions of plane strain, the Tresca yield criterion may be written as

$$F = (\sigma_x - \sigma_z)^2 + 4\tau_{xz}^2 - 4c_u^2 = 0$$

where compression is taken as positive and c_u may depend linearly on z . In terms of the quantities $(\sigma_x - \sigma_z)$ and $2\tau_{xz}$, this function plots as a circle of radius $2c_u$ as shown in Figure 5.

To define a rigorous lower bound, the stresses at each point in the grid must lie inside the Tresca circle so that $F \leq 0$. Since this type of constraint is nonlinear, it is convenient to replace the Tresca circle by an inscribed polygon with p sides of equal length so that the yield criterion can be expressed as a series of linear inequalities.

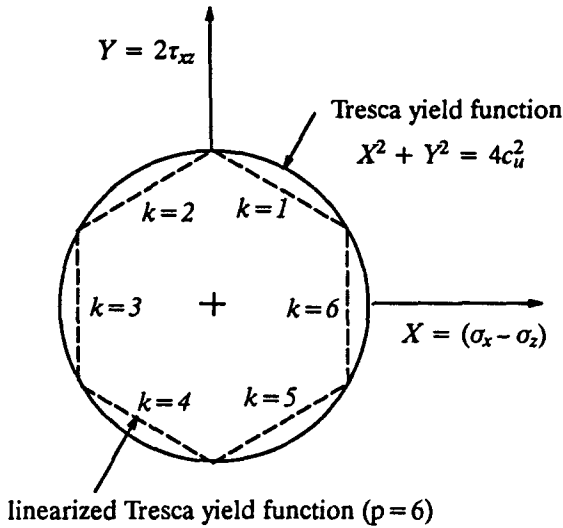


Figure 5: Internal linear approximation to Tresca yield function

With reference to Figure 5, which shows a six-sided approximation, the linearized yield criterion is given by

$$F_k = A_k \sigma_x + B_k \sigma_z + C_k \tau_{xz} - 2c_u \cos(\pi/p) \leq 0$$

where

$$A_k = \cos(2\pi k/p) \quad ; \quad B_k = -A_k \quad ; \quad C_k = 2 \sin(2\pi k/p)$$

and k ranges from 1 to p . As each side of the the polygonal yield surface is linear in the unknown stresses, the above equation needs to be enforced at each node of each triangular element. This gives rise to a set of p inequality constraints of the form

$$\mathbf{a}_5 \mathbf{x} \leq b_5 \quad (8)$$

where \mathbf{a}_5 is comprised of the coefficients A_k , B_k and C_k , $\mathbf{x} = \{\sigma_{xi}, \sigma_{zi}, \tau_{xzi}\}^T$ is the stress vector for node i , and $b_5 = 2c_u \cos(\pi/p)\{1, 1, \dots, 1\}^T$.

For the four-noded rectangular extension element of Figure 3, constraints of the form of equation (8) apply at nodes 2 and 3 but, at node 1, a slightly different set of inequalities need to be enforced. If F_{ki} denotes the value of the k th side of the yield function at node i , then it may be shown that the yield condition is satisfied everywhere in the extension zone by imposing the inequality constraint $F_{k1} \leq F_{k2}$. This leads to the following set of constraints

$$\mathbf{a}_6 \mathbf{x} \leq b_6 \quad (9)$$

where \mathbf{a}_6 is comprised of the coefficients A_k , B_k and C_k , $\mathbf{x} = \{\sigma_{x1}, \sigma_{z1}, \tau_{xz1}, \sigma_{x2}, \sigma_{z2}, \tau_{xz2}\}^T$ and $\mathbf{b}_6 = \{0, \dots, 0\}^T$.

For the three-noded triangular extension element, it may be shown that we need to apply the constraints $F_{k1} \leq F_{k2}$, $F_{k3} \leq F_{k2}$ and $F_{k2} \leq 0$ to ensure that the linearized yield criterion is not violated. The first two of these constraints are of the form of equation (9) whereas the last constraint is of the same type as equation (8).

To formulate the lower bound theorem as a linear programming problem, it is necessary to define an objective function. For most plane strain geotechnical problems, we seek a statically admissible stress field which maximizes an integral of the normal stress σ_n over some part of the boundary. This integral corresponds to the collapse load and is expressed in terms of the unknown stresses. Since the stress distribution is linear, the integration can be performed analytically for each boundary segment to give

$$Q = \frac{L}{2}(\sigma_{n1} + \sigma_{n2}) = \mathbf{c}^T \mathbf{x} \quad (10)$$

where Q is the collapse load per unit thickness, L is the length of the boundary segment and $(\sigma_{n1}, \sigma_{n2})$ are the normal stresses at its two ends. The objective function coefficients \mathbf{c} are constants which depend on the orientation and length of each segment and \mathbf{x} is a vector of cartesian stresses for the two end nodes.

Once the elemental constraint matrices and objective function coefficients have been found using equations (4)–(10), the various terms may be assembled (by the usual finite element procedure) to furnish the lower bound linear programming problem. The task of finding a statically admissible stress field, which maximizes the collapse load over a specified area, may be written as

$$\begin{array}{ll} \text{Minimize} & -\mathbf{C}^T \mathbf{X} \\ \text{Subject to} & \mathbf{A}_1 \mathbf{X} = \mathbf{B}_1 \\ & \mathbf{A}_2 \mathbf{X} = \mathbf{B}_2 \\ & \mathbf{A}_3 \mathbf{X} = \mathbf{B}_3 \\ & \mathbf{A}_4 \mathbf{X} = \mathbf{B}_4 \\ & \mathbf{A}_5 \mathbf{X} \leq \mathbf{B}_5 \\ & \mathbf{A}_6 \mathbf{X} \leq \mathbf{B}_6 \end{array} \quad (11)$$

where \mathbf{X} is the global vector of unknown nodal stresses. This type of linear optimization problem is unusual since all of the variables are unbounded and, for most cases, the overall constraint matrix has many more rows than columns. A detailed discussion of the various alternatives for solving equation (11) may be found in Sloan [1] and will not be repeated

here. It suffices to note that an active set algorithm, developed by Sloan [2], is particularly efficient since it fully exploits the extreme sparsity of the constraints and permits very large analyses to be conducted on a workstation or microcomputer.

NUMERICAL FORMULATION OF THE UPPER BOUND THEOREM

One of the earliest investigations of a numerical formulation for the upper bound theorem, which employed finite elements in conjunction with linear programming, may be found in Anderheggen and Knopf [4]. This work focused on the collapse of plates and gives an extensive discussion of alternative procedures. Using a similar approach, Bottero *et al.* [6] included the effects of velocity discontinuities and applied the method to a variety of soil mechanics problems. More recently, Sloan [7] has proposed a formulation based on duality theory which employs a steepest edge active set algorithm to solve the resulting linear programming problem efficiently. The upper bound method, like the lower bound method, typically leads to very large optimization problems involving several thousand variables and constraints, and it is essential to fully exploit the extreme sparsity of the constraint matrix.

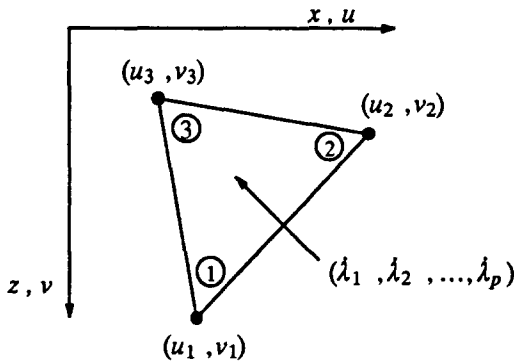
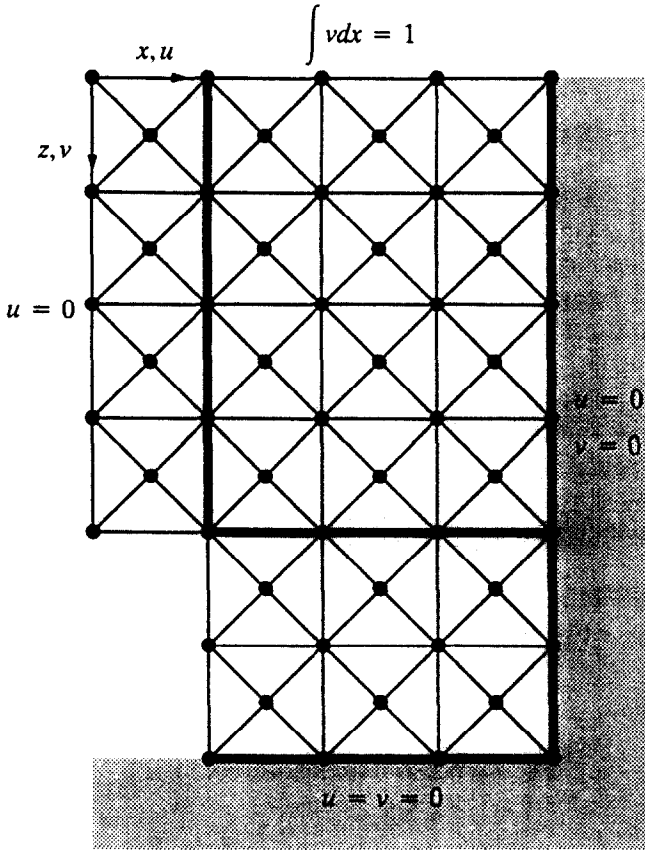


Figure 6: Element for upper bound limit analysis

The three-noded triangle used in the upper bound formulation is shown in Figure 6. Each node has two velocity components and each element has p plastic multiplier rates (where p is the number of sides in the linearized yield criterion). The velocities are assumed to vary linearly across each element according to

$$u = \sum_{i=1}^{i=3} N_i u_i \quad ; \quad v = \sum_{i=1}^{i=3} N_i v_i \quad (12)$$

where N_i are shape functions and (u_i, v_i) are the nodal velocities in the x - and z - directions respectively. A simple upper bound mesh for a square tunnel, which includes four velocity discontinuities, is shown in Figure 7.



88 triangular elements
 4 velocity discontinuities
 16 velocity discontinuity segments

Figure 7: Illustrative upper bound mesh for square tunnel

To be kinematically admissible, and thus provide a rigorous upper bound on the exact collapse load, the velocity field must satisfy the flow rule. For plane strain deformation of a rigid plastic soil, the plastic strain rates are given by

$$\dot{\epsilon}_x = -\frac{\partial u}{\partial x} = \dot{\lambda} \frac{\partial F}{\partial \sigma_x} \quad ; \quad \dot{\epsilon}_z = -\frac{\partial v}{\partial z} = \dot{\lambda} \frac{\partial F}{\partial \sigma_z} \quad ; \quad \dot{\gamma}_{xz} = -\left(\frac{\partial v}{\partial x} + \frac{\partial u}{\partial z}\right) = \dot{\lambda} \frac{\partial F}{\partial \tau_{xz}} \quad (13)$$

where $\dot{\lambda} \geq 0$ is a plastic multiplier rate and compressive strains are taken as positive. These equations, together with the boundary conditions and flow rule relations for the velocity discontinuities, define a kinematically admissible velocity field. To remove the stress terms from the flow rule equations, and thus provide a linear relationship between

the unknown velocities and plastic multiplier rates, it is again necessary to derive a linear approximation to the Tresca yield surface. Unlike the static method, which uses an internal

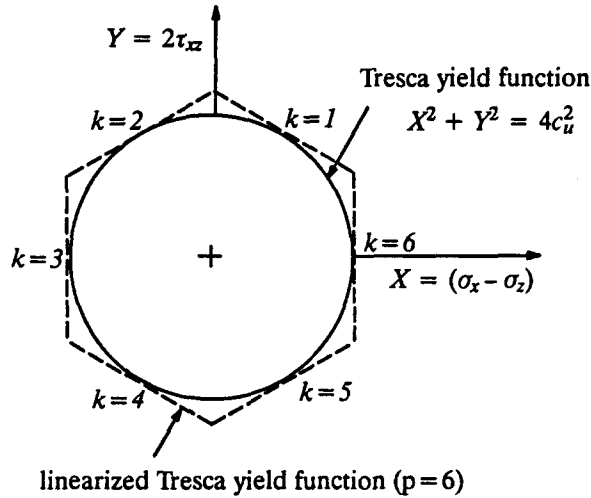


Figure 8: External linear approximation to Tresca yield function

polygon, the upper bound method uses an external polygon as shown in Figure 8. This polygon has p sides of equal length and is defined according to

$$F_k = A_k \sigma_x + B_k \sigma_z + C_k \tau_{xz} - 2c_u = 0 \quad (14)$$

where A_k , B_k , and C_k are the same as for the lower bound linearization and k ranges from 1 to p . Differentiating equation (12), and using equations (13) and (14), the flow rule constraints are obtained as

$$\begin{aligned} \sum_{i=1}^{i=3} \frac{\partial N_i}{\partial x} u_i + \sum_{k=1}^{k=p} \lambda_k A_k &= 0 \\ \sum_{i=1}^{i=3} \frac{\partial N_i}{\partial z} v_i + \sum_{k=1}^{k=p} \lambda_k B_k &= 0 \\ \sum_{i=1}^{i=3} \frac{\partial N_i}{\partial x} v_i + \sum_{i=1}^{i=3} \frac{\partial N_i}{\partial z} u_i + \sum_{k=1}^{k=p} \lambda_k C_k &= 0 \end{aligned}$$

where each of the plastic multiplier rates $\lambda_k \geq 0$. When applied to each element, the general form of these constraints is

$$\mathbf{a}_{11} \mathbf{x}_1 + \mathbf{a}_{12} \mathbf{x}_2 = \mathbf{b}_1 \quad (15)$$

where \mathbf{a}_{11} and \mathbf{a}_{12} are matrices of constants, $\mathbf{b}_1 = \{0, 0, 0\}^T$, $\mathbf{x}_1 = \{u_1, v_1, u_2, v_2, u_3, v_3\}^T$, and $\mathbf{x}_2 = \{\lambda_1, \dots, \lambda_p\}^T$ with $\mathbf{x}_2 \geq 0$.

To permit kinematically admissible velocity discontinuities in the formulation, two additional constraints need to be imposed on the velocity field. The first of these arises from a specified sign condition which ensures that the power dissipated by relative sliding along a discontinuity is nonnegative. The second type of constraint is required to enforce the flow rule. If u_t denotes the jump in the tangential velocity, the sign condition is defined so that $|u_t| = s u_t$, where $s = \pm 1$ and is specified. Using the definition for u_t , with the condition that $s u_t \geq 0$, leads to an inequality of the general form

$$\mathbf{a}_2 \mathbf{x}_1 \leq \mathbf{b}_2 \quad (16)$$

where \mathbf{a}_2 is a function of s and the orientation of the discontinuity, $\mathbf{x}_1 = \{u_1, v_1, u_2, v_2\}^T$ and $\mathbf{b}_2 = 0$. This constraint is applied to each pair of nodes on a discontinuity so that the tangential velocity is always of the same sign along its length. The flow rule condition is $u_n = 0$, where u_n is the jump in normal velocity. Substituting the expression for u_n gives an equality constraint of the form

$$\mathbf{a}_3 \mathbf{x}_1 = \mathbf{b}_3 \quad (17)$$

in which \mathbf{a}_3 is a function of the orientation of the discontinuity, $\mathbf{x}_1 = \{u_1, v_1, u_2, v_2\}^T$, and $\mathbf{b}_3 = 0$.

The final type of constraint to be imposed on the velocity field arises from the boundary conditions. Boundary conditions are specified at selected nodes and, for the general case, may be written as

$$\mathbf{a}_4 \mathbf{x}_1 = \mathbf{b}_4 \quad (18)$$

where \mathbf{a}_4 is a matrix of constants which depend on the orientation of the relevant boundary, \mathbf{b}_4 is a vector of prescribed values, and $\mathbf{x}_1 = \{u_i, v_i\}^T$ for node i .

To complete the upper bound formulation, it is necessary to define the objective function. Since we wish to compute a kinematically admissible velocity field which minimizes the internal power dissipation, we need to express this quantity in terms of the unknown velocities and plastic multiplier rates. The power dissipated per unit thickness in the out-of-plane direction, by sliding along a discontinuity, is given by

$$P_d = \int_L c_u |u_t| dL$$

where c_u may vary linearly with z and L is the length of the discontinuity segment. By substituting the expression for u_t with the specified sign condition $|u_t| = s u_t$, this

equation may be integrated to give P_d in terms of the nodal velocities according to

$$P_d = sL \left[u_{t1} \left(\frac{c_{u1}}{3} + \frac{c_{u2}}{6} \right) + u_{t2} \left(\frac{c_{u1}}{6} + \frac{c_{u2}}{3} \right) \right] = \mathbf{c}_1^T \mathbf{x}_1 \quad (19)$$

in which (c_{u1}, c_{u2}) and (u_{t1}, u_{t2}) are the nodal shear strengths and tangential velocity jumps, respectively, at each end of the discontinuity and $\mathbf{x}_1 = \{u_1, v_1, \dots, u_4, v_4\}^T$. The power dissipated by plastic deformation throughout each triangular element is defined as

$$P_t = \int_A (\sigma_x \dot{\epsilon}_x + \sigma_z \dot{\epsilon}_z + \tau_{xz} \dot{\gamma}_{xz}) dA$$

where a unit out-of-plane thickness is assumed and A is the triangle area. Substituting (13) and (14) permits P_t to be expressed in terms of the plastic multiplier rates according to

$$P_t = \frac{2}{3} (c_{u1} + c_{u2} + c_{u3}) A \sum_{k=1}^{k=p} \dot{\lambda}_k = \mathbf{c}_2^T \mathbf{x}_2 \quad (20)$$

in which \mathbf{c}_2 is a function of A and c_{u1}, c_{u2}, c_{u3} (the nodal values of c_u), and $\mathbf{x}_2 = \{\dot{\lambda}_1, \dots, \dot{\lambda}_p\}^T$.

Once the elemental constraint matrices and objective function coefficients have been found using equations (15)–(20), the various terms may be assembled in the usual way to furnish the upper bound linear programming problem. The task of finding a kinematically admissible velocity field, which minimizes the internal power dissipation for a specified set of boundary conditions, may be written as

$$\begin{array}{ll} \text{Minimize} & \mathbf{C}_1^T \mathbf{X}_1 + \mathbf{C}_2^T \mathbf{X}_2 \\ \text{Subject to} & \mathbf{A}_{11} \mathbf{X}_1 + \mathbf{A}_{12} \mathbf{X}_2 = \mathbf{B}_1 \\ & \mathbf{A}_2 \mathbf{X}_1 \leq \mathbf{B}_2 \\ & \mathbf{A}_3 \mathbf{X}_1 = \mathbf{B}_3 \\ & \mathbf{A}_4 \mathbf{X}_1 = \mathbf{B}_4 \\ & \mathbf{X}_2 \geq 0 \end{array} \quad (21)$$

where for a mesh with n nodes and e triangles, with $m = pe$, $\mathbf{X}_1 = \{u_1, v_1, \dots, u_n, v_n\}^T$ and $\mathbf{X}_2 = \{\dot{\lambda}_1, \dots, \dot{\lambda}_m\}^T$. A detailed analysis of various strategies for solving this type of linear programming problem may be found in Sloan [7]. One very efficient approach is not to solve (21) directly but, rather, to solve its dual. The dual linear programming

problem is ideally suited to solution by the same active set algorithm that is used for the lower bound linear programming problem.

RESULTS

In the most common type of loading, collapse of the tunnel of Figure 1 is triggered by the action of gravity with the internal tunnel pressure providing resistance to failure. For plane strain conditions where the soil flows into the cavity, the external power dissipation per unit thickness may be expressed as

$$P_{ext} = (\sigma_s - \sigma_t) \int_{z=0} v dx + \gamma \int_A \int v dx dz \quad (22)$$

where A is the area of the soil mass which deforms at constant volume. This equation may also be written in terms of the dimensionless parameters $(\sigma_s - \sigma_t)/c_{u0}$ and $\gamma B/c_{u0}$ according to

$$P_{ext} = \left(\frac{\sigma_s - \sigma_t}{c_{u0}} \right) \left[c_{u0} \int_{z=0} v dx \right] + \left(\frac{\gamma B}{c_{u0}} \right) \left[\frac{c_{u0}}{B} \int_A \int v dx dz \right] \quad (23)$$

These two quantities provide a convenient means for summarizing the stability of the tunnel and are commonly known as "stability numbers". They are both functions of H/B and $\rho B/c_{u0}$. In most design situations, it is necessary to be able to determine the maximum value of $(\sigma_s - \sigma_t)/c_{u0}$ for given values of H/B , $\rho B/c_{u0}$ and $\gamma B/c_{u0}$.

A typical lower bound mesh, for $H/B = 5$ and $\gamma B/c_{u0} = 5$, is shown in Figure 9. The grid has 1623 nodes, 508 triangles, 1 triangular extension element, 24 rectangular extension elements and 784 stress discontinuities. The arrangement of the extension elements ensures that the stress field can be extended throughout the semi-infinite domain of the problem without violating equilibrium, the stress boundary conditions or the yield criterion. This property guarantees that the solution is a true lower bound on the exact collapse load. To perform the actual lower bound computation, we first prescribe values for H/B , $\rho B/c_{u0}$, σ_s and $\gamma B/c_{u0}$ and then solve (11) to find a statically admissible stress field which maximizes a uniform tensile stress over the face of the tunnel. For a 12-sided approximation to the Tresca yield surface, with $\rho B/c_{u0} = 0.5$, the mesh of Figure 9 gives a lower bound of $(\sigma_s - \sigma_t)/c_{u0} = -13.88$.

A typical upper bound mesh, also for the case of $H/B = 5$ and $\gamma B/c_{u0} = 5$, is shown in Figure 10. The grid has 2 vertical discontinuities and 2 horizontal discontinuities and the boundary conditions are as shown. In total, there are 666 nodes and 1120 triangles. To compute an upper bound for $(\sigma_s - \sigma_t)/c_{u0}$, we first select values for H/B , $\rho B/c_{u0}$ and

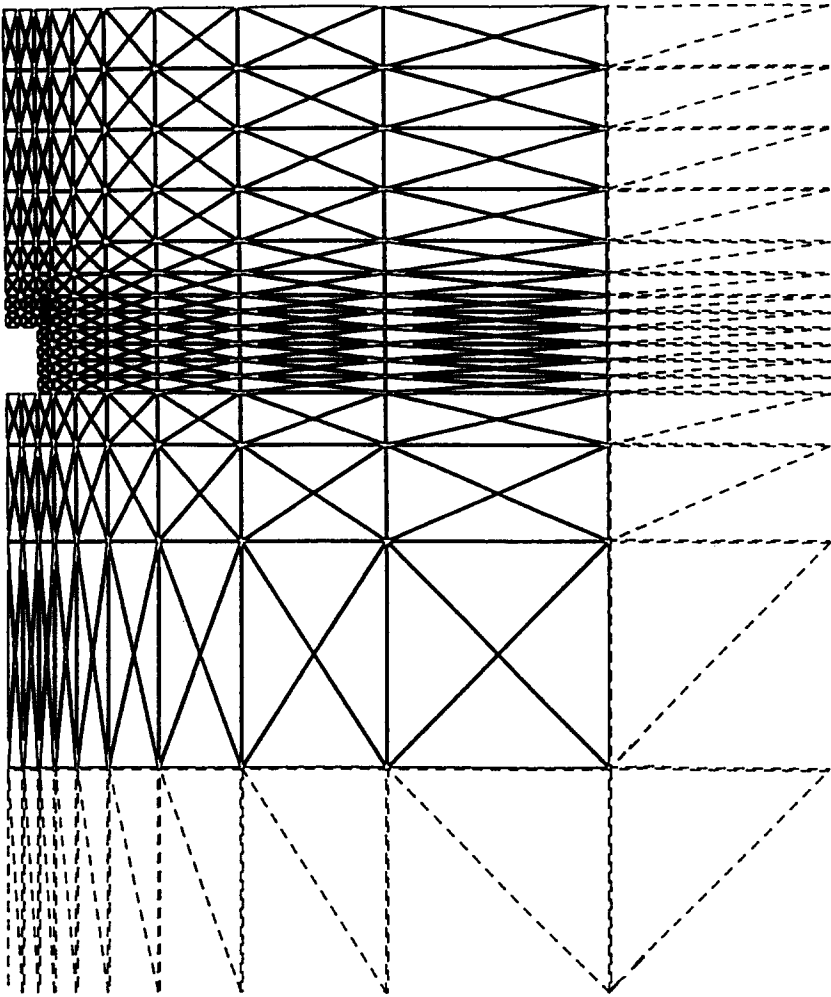


Figure 9: Lower bound mesh for square tunnel with $H/B = 5$ and $\gamma B/c_{u0} = 5$

$\gamma B/c_{u0}$, and then set the integral of the downward velocity along the ground surface equal to unity. Because the plastic deformations associated with the Tresca yield condition occur at constant volume, the integral of the velocities normal to the tunnel face must be equal and opposite to the integral of the normal velocities at the ground surface. Before solving (21), we equate the power expended by the external loads to the power dissipated internally and then subtract the second integral in equation (22) from both sides. This creates additional terms in the objective function, but permits $(\sigma_s - \sigma_t)/c_{u0}$ to be minimized directly. For the mesh of Figure 10, with a 12-sided approximation to the yield surface and the same properties as before, the finite element method furnishes an upper

bound on $(\sigma_s - \sigma_t)/c_{u0}$ of -12.48 . When combined with the lower bound result obtained previously, the exact collapse load has thus been bracketed to within about 10 percent. The kinematically admissible velocity field for this upper bound calculation is shown in Figure 11.

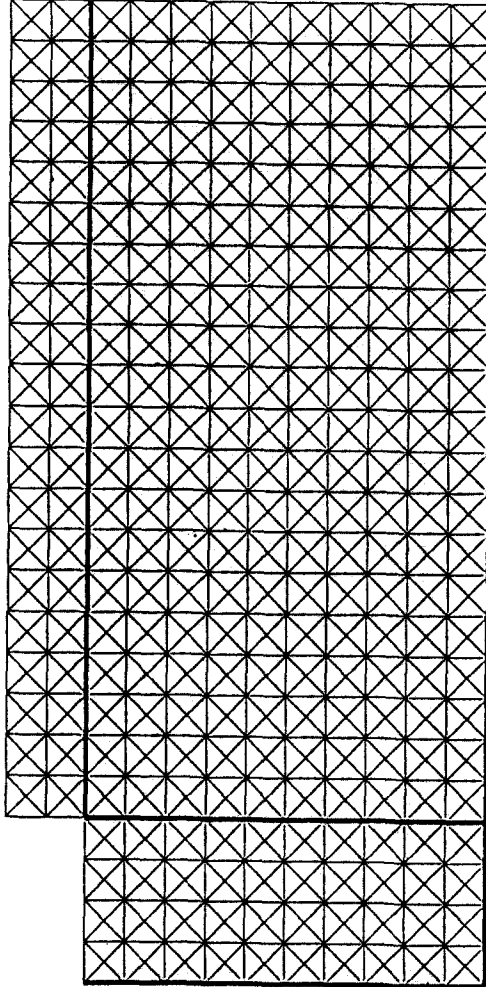


Figure 10: Upper bound mesh for square tunnel with $H/B = 5$ and $\gamma B/c_{u0} = 5$

To provide an additional check on the upper bound results, the rigid block mechanisms shown in Figures 12 and 13 were also used to estimate the tunnel collapse pressures. These models permit plastic deformation to occur only at the interfaces between adjacent blocks, which act as velocity discontinuities. The simple trapdoor mechanism of Figure 12 assumes

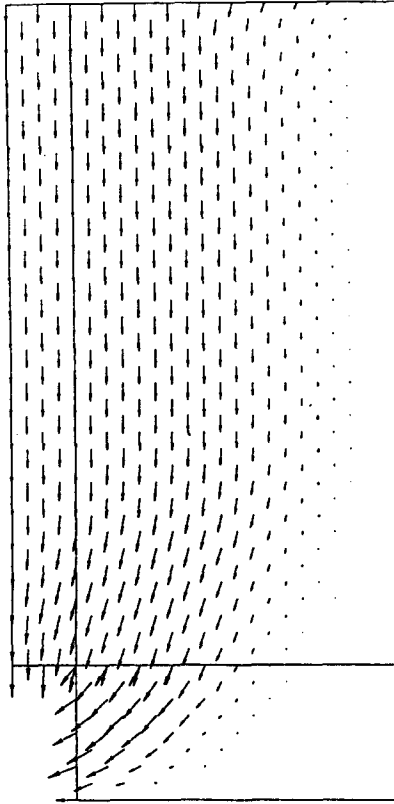


Figure 11: Velocity field for square tunnel with $H/B = 5$, $\rho B/c_{u0} = 0.5$ and $\gamma B/c_{u0} = 5$

that collapse occurs solely by uniform deformation of the roof, and is applicable to very shallow tunnels where the true collapse mode is quite localized. Equating the internal and external power dissipation for this arrangement gives an upper bound on $(\sigma_s - \sigma_t)/c_{u0}$ as

$$\left(\frac{\sigma_s - \sigma_t}{c_{u0}} \right) \leq \left(\frac{H}{B} \right) \left(2 + \frac{\rho H}{c_{u0}} - \frac{\gamma B}{c_{u0}} \right) \quad (24)$$

For deeper tunnels, collapse invariably causes surface deformations over a wider area and an alternative mechanism, such as that shown in Figure 13, needs to be used. This model permits movement of both the walls and roof and its geometry is completely defined by the three angles (α, β, δ) . The best upper bound for this mechanism is found by first equating the rate of work done by the external loads to the internal power dissipation so that $(\sigma_s - \sigma_t)/c_{u0}$ may be expressed in terms of the quantities H/B , $\rho B/c_{u0}$, $\gamma B/c_{u0}$ and

the three variable angles. The geometry of the blocks is then optimised, by searching for the critical combination of (α, β, δ) , to furnish the minimum value for $(\sigma_s - \sigma_t)/c_{u0}$. For a tunnel with $H/B = 5$, $\gamma B/c_{u0} = 5$ and $\rho B/c_{u0} = 0.5$, the 3-variable mechanism gives an upper bound for $(\sigma_s - \sigma_t)/c_{u0}$ of -12.50. This bound is slightly better than the value of -12.48 obtained from the finite element mesh of Figure 10.

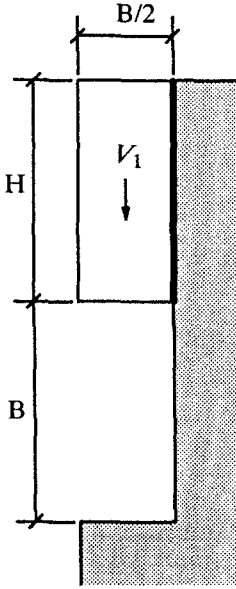


Figure 12: Trapdoor mechanism

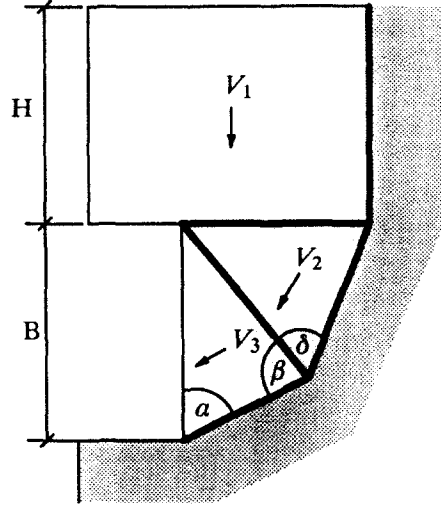


Figure 13: 3-variable mechanism

A complete set of stability bounds on $(\sigma_s - \sigma_t)/c_{u0}$, for various values of H/B , $\rho B/c_{u0}$ and $\gamma B/c_{u0}$, is shown in Table 1. This Table includes upper and lower bounds for the case of $\rho B/c_{u0} = 0$, which corresponds to a tunnel in a soil with uniform undrained shear strength $c_u = c_{u0}$. The results for all of the analyses are presented in the form of dimensionless stability charts in Figures 14 to 18. Except for examples where the the load parameter $(\sigma_s - \sigma_t)/c_{u0}$ approaches zero, the upper and lower bounds differ typically by less than 15 percent and are thus certainly precise enough for the purposes of design. The meshes for the various finite element computations were found by a trial-and-error procedure and a 12-sided linearization of the Tresca yield surface was used in all of the analyses. Numerical experiments suggest that increasing the accuracy of the yield surface approximation, by doubling the number of sides to 24, affects the computed bounds by less than a few percent.

Since the statically admissible stress fields are based on analysis with a convex yield surface, it follows that the boundary of the safe load region, when plotted in terms of the

		$(\sigma_s - \sigma_t)$											
		c_{u0}											
$\frac{H}{B}$	$\frac{\rho B}{c_{u0}}$	$\frac{\gamma B}{c_{u0}} = 0$		$\frac{\gamma B}{c_{u0}} = 1$		$\frac{\gamma B}{c_{u0}} = 2$		$\frac{\gamma B}{c_{u0}} = 3$		$\frac{\gamma B}{c_{u0}} = 4$		$\frac{\gamma B}{c_{u0}} = 5$	
1	0	1.88	2.00	0.81	0.95	-0.44	-0.27	-1.83	-1.59	-3.25	-2.97	-4.74	-4.38
	0.25	2.12	2.25		1.25		0.25		-0.93		-2.20	-3.85	-3.56
	0.5	2.36	2.50		1.50		0.50		-0.50		-1.60	-3.19	-2.84
	0.75	2.60	2.75		1.75		0.75		-0.25		-1.25	-2.63	-2.28
	1	2.85	3.00		2.00		1.00		0.00		-1.00	-2.17	-2.00
2	0	2.89	3.15	0.60	0.83	-1.78	-1.51	-4.22	-3.90	-6.73	-6.32	-9.36	-8.77
	0.25	4.08	4.43		2.20		-0.11		-2.43		-4.75	-7.57	-7.10
	0.5	5.21	5.64		3.49		1.24		-1.06		-3.37	-6.16	-5.69
	0.75	6.25	6.79		4.68		2.53		0.29		-2.02	-4.81	-4.33
	1	7.24	7.91		5.84		3.73		1.57		-0.67	-3.54	-2.97
3	0	3.46	3.82	0.14	0.48	-3.24	-2.87	-6.73	-6.27	-10.20	-9.70	-13.60	-13.16
	0.25	5.60	6.12		2.80		-0.53		-3.87		-7.20	-11.16	-10.54
	0.5	7.62	8.38		5.07		1.75		-1.58		-4.90	-8.90	-8.23
	0.75	9.66	10.62		7.32		4.00		0.69		-2.63	-6.71	-5.96
	1	11.68	12.83		9.56		6.25		2.94		-0.38	-4.59	-3.70
4	0	3.90	4.31	-0.41	0.01	-4.83	-4.38	-9.38	-8.79	-13.81	-13.23	-18.40	-17.71
	0.25	7.00	7.73		3.47		-0.85		-5.19		-9.54	-14.69	-13.89
	0.5	10.05	11.09		6.85		2.52		-1.82		-6.15	-11.44	-10.49
	0.75	13.10	14.43		10.19		5.86		1.53		-2.80	-8.35	-7.14
	1	16.15	17.75		13.52		9.19		4.87		0.54	-5.20	-3.79
5	0	4.23	4.73	-1.06	-0.59	-6.51	-5.96	-12.10	-11.36	-17.60	-16.80	-23.20	-22.28
	0.25	8.45	9.36		4.09		-1.20		-6.51		-11.85	-18.18	-17.20
	0.5	12.56	13.93		8.77		3.41		-1.87		-7.17	-13.88	-12.50
	0.75	16.67	18.47		13.23		7.98		2.71		-2.57	-9.73	-7.90
	1	20.77	23.01		17.78		12.53		7.27		2.00	-5.60	-3.33

Table 1: Stability bounds for $(\sigma_s - \sigma_t)/c_{u0}$

- Notes: 1. **Bold entries** indicate upper bounds from 3-variable mechanism
2. **Blank entries** for lower bounds can be found by linear interpolation along rows using values at $\gamma B/c_{u0} = 0$ and $\gamma B/c_{u0} = 5$

load parameters $(\sigma_s - \sigma_t)/c_{u0}$ and $\gamma B/c_{u0}$, is also convex. This feature of the lower bound curves permits a parametric study to be done without computing lower bounds for all combinations of H/B , $\rho B/c_{u0}$, and $\gamma B/c_{u0}$. Except for cases where $\rho B/c_{u0} = 0$, Table

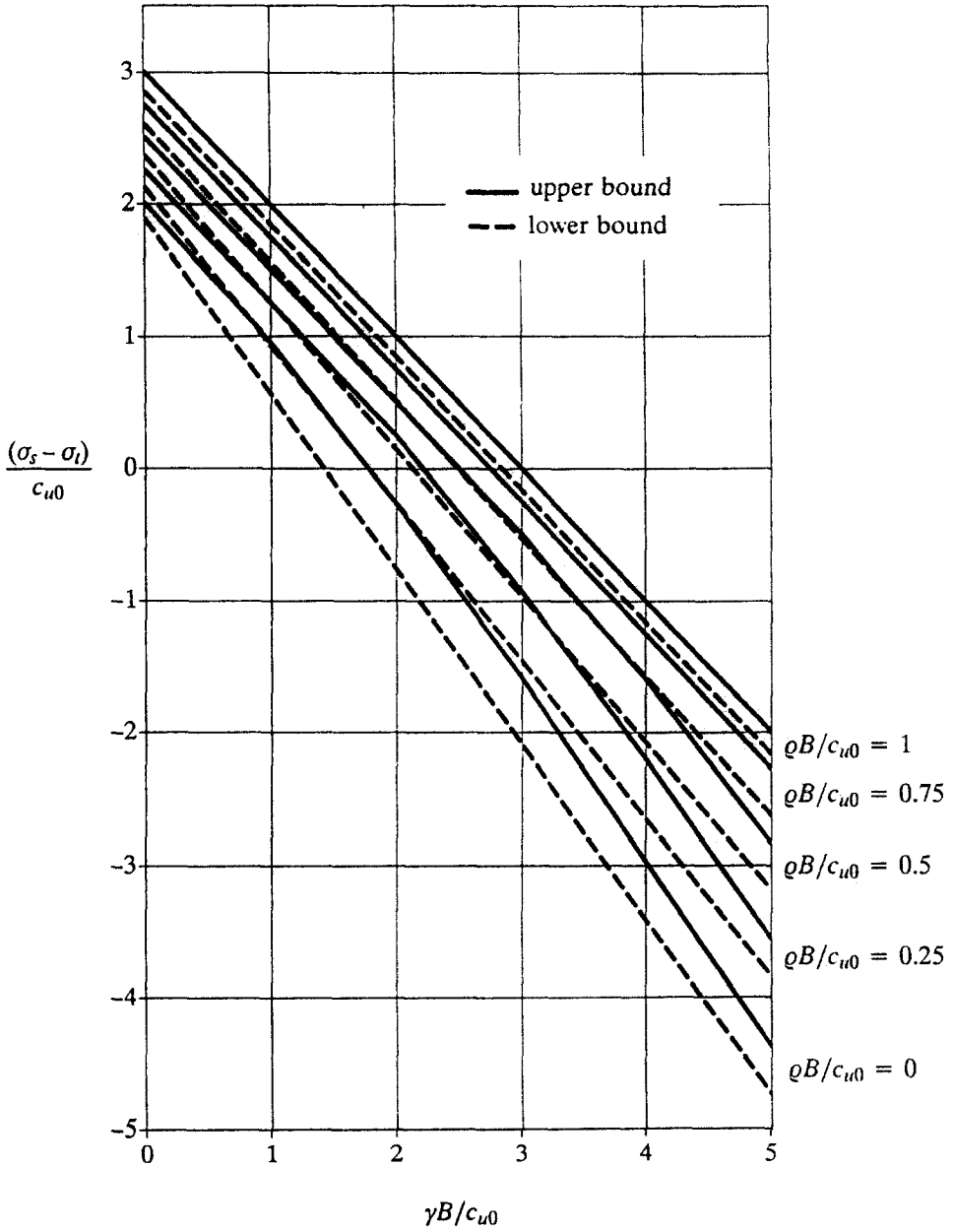


Figure 14: Stability bounds for square tunnel with $H/B = 1$

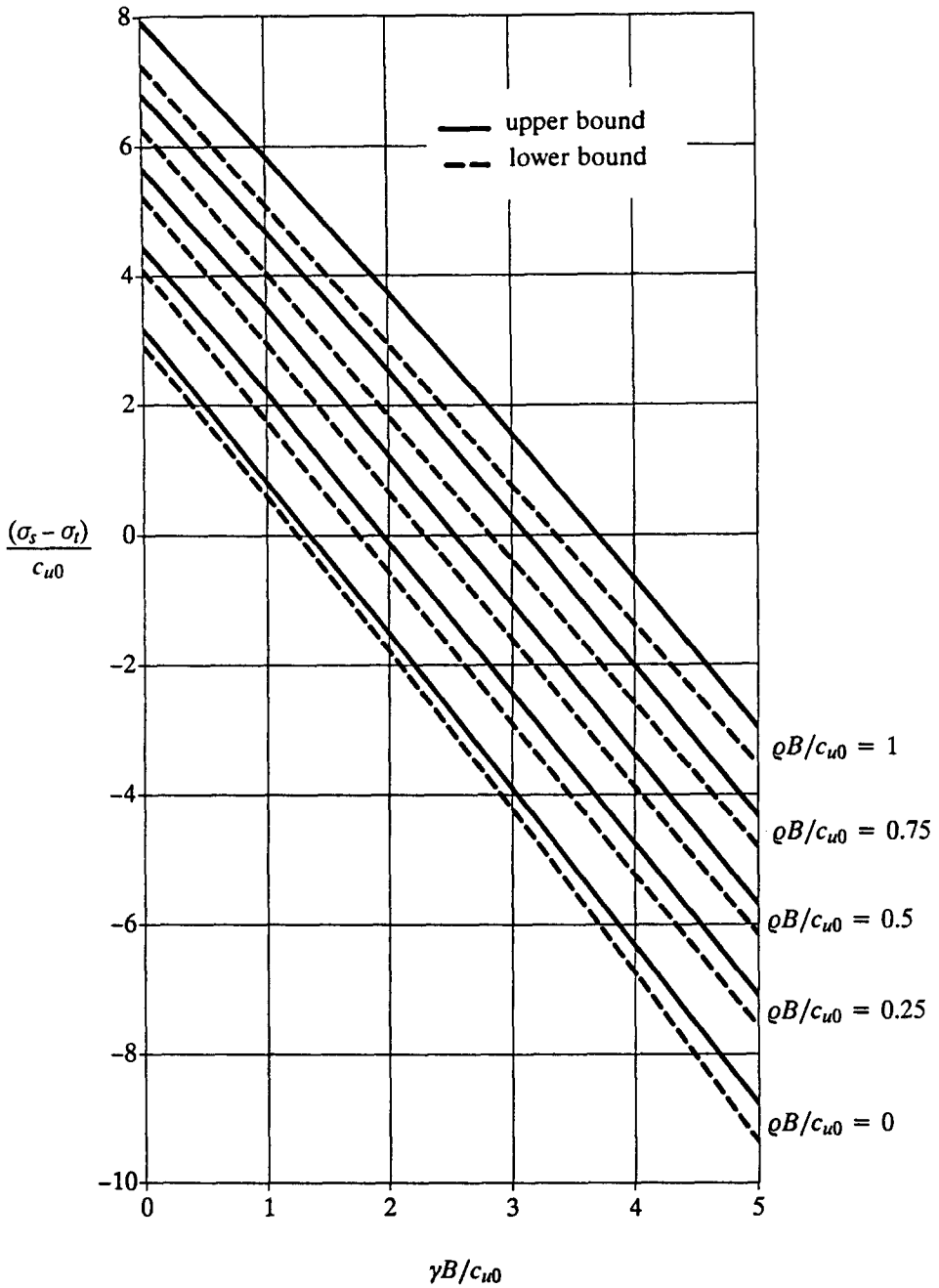


Figure 15: Stability bounds for square tunnel with $H/B = 2$

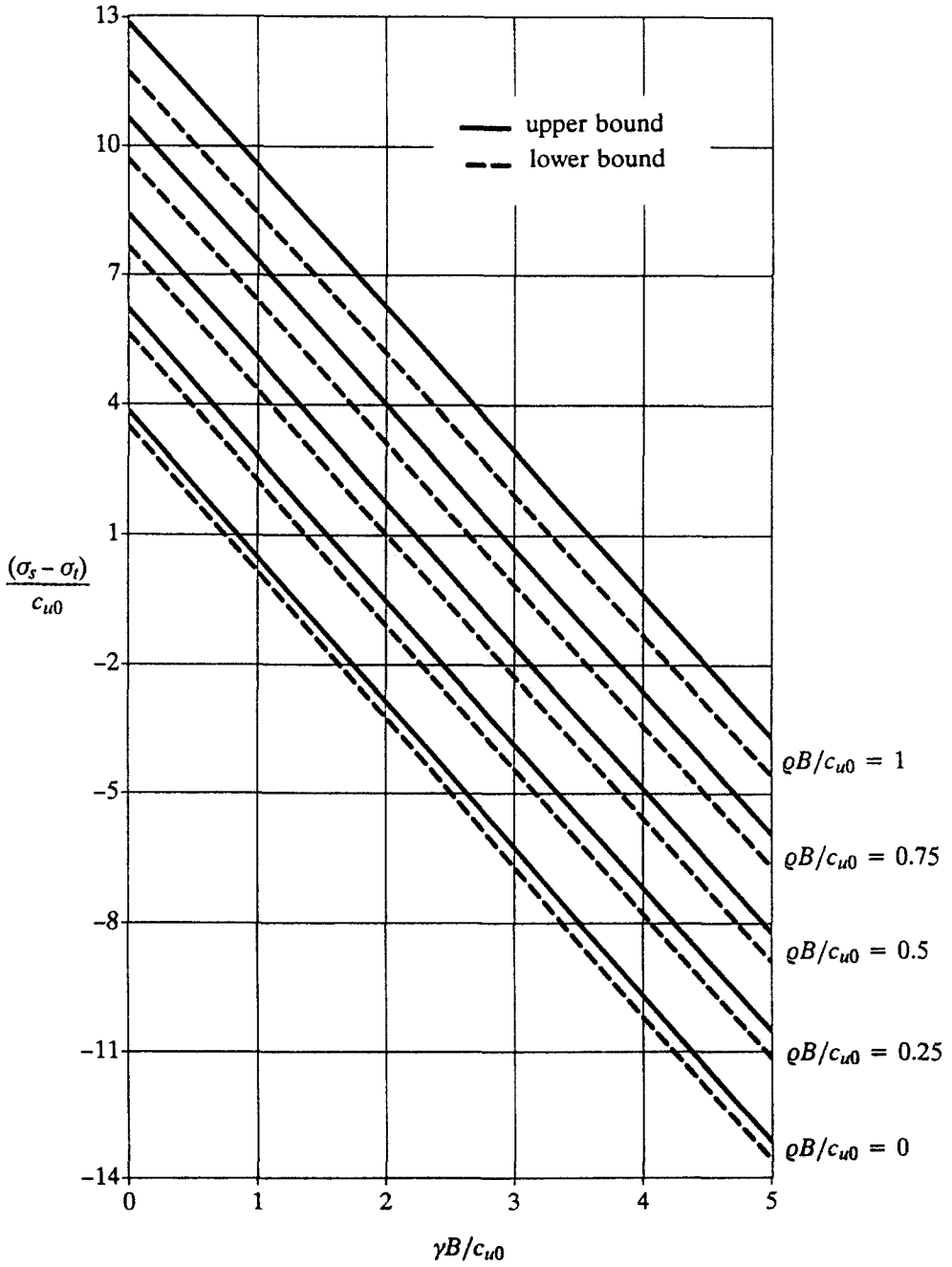


Figure 16: Stability bounds for square tunnel with $H/B = 3$

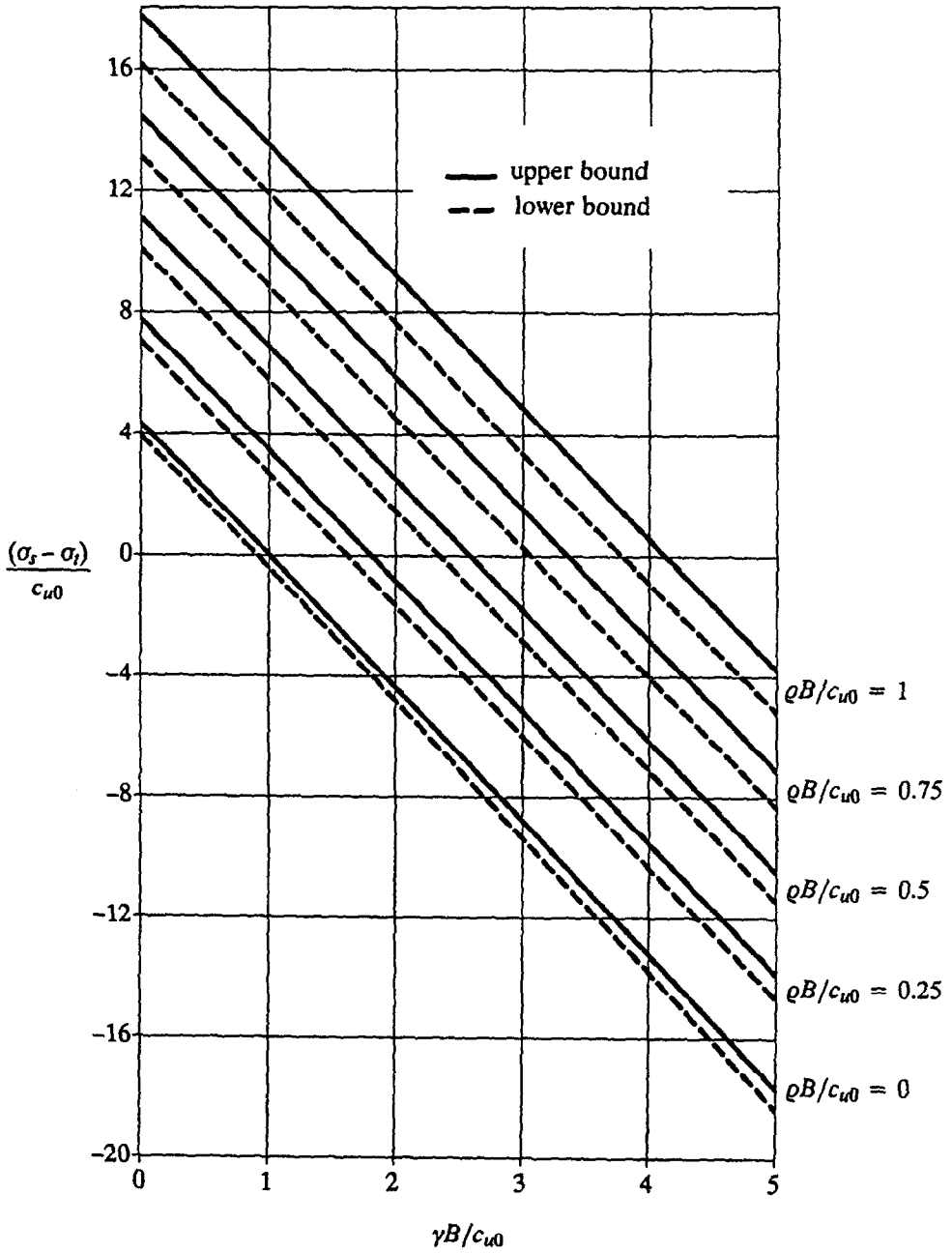


Figure 17: Stability bounds for square tunnel with $H/B = 4$

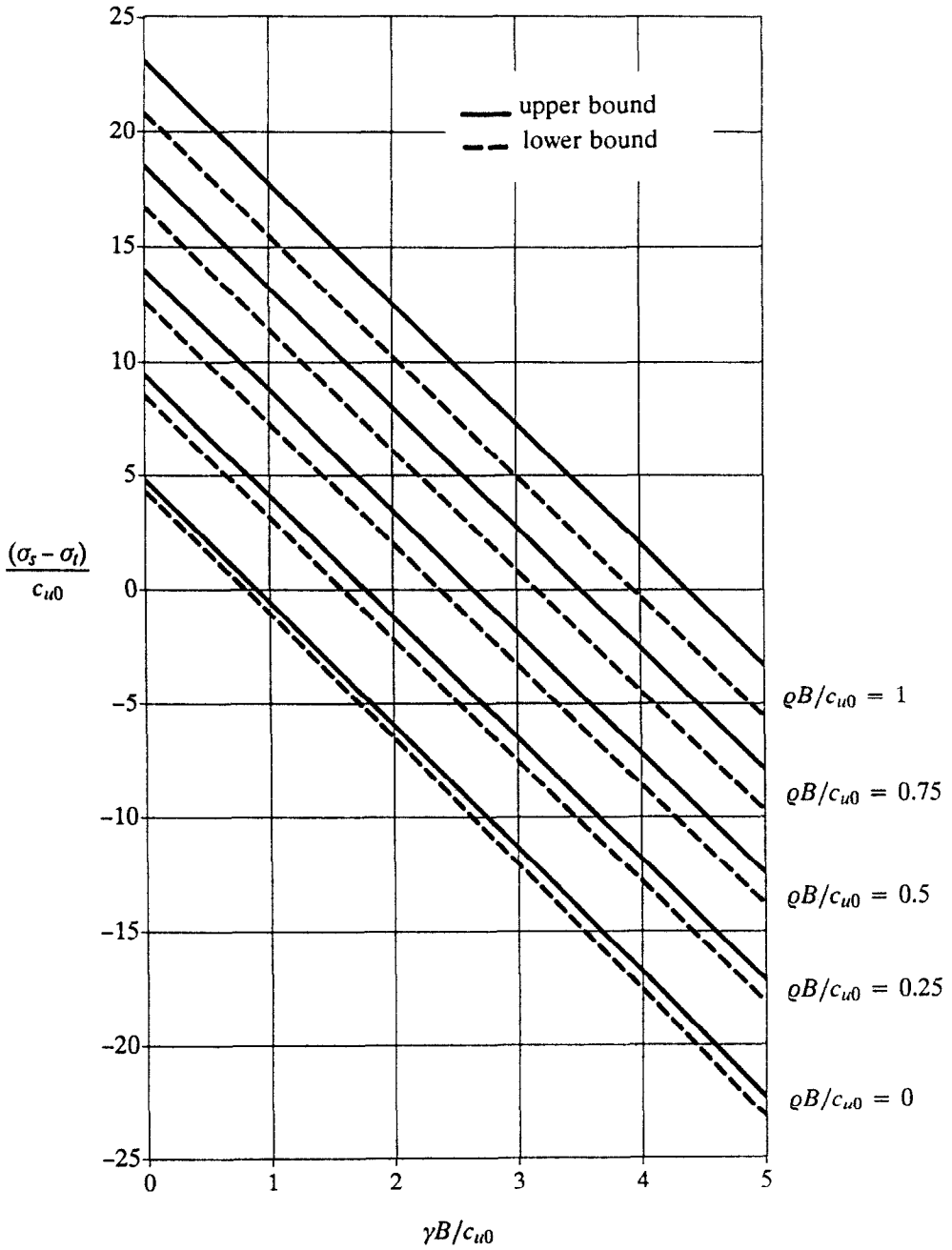


Figure 18: Stability bounds for square tunnel with $H/B = 5$

1 only gives lower bounds on $(\sigma_s - \sigma_t)/c_{u0}$ for $\gamma B/c_{u0} = 0$ and $\gamma B/c_{u0} = 5$. Rigorous lower bounds for the remaining entries in each row of the Table can be found by using linear interpolation with these values. The accuracy of this approach, for all cases with $\rho B/c_{u0} = 0$, may be verified readily by comparing interpolated values against the complete set of lower bounds shown.

For very shallow tunnels, we would expect the trapdoor mechanism and the kinematic finite element method to give the same upper bounds on $(\sigma_s - \sigma_t)/c_{u0}$. The results in Table 1 indicate that this is indeed true for many of the cases where $H/B = 1$. When $H/B < 1$, the trapdoor mode of failure is undoubtedly very close to the true mode of failure, and the upper bound of equation (24) is a good approximation to the exact solution. The bold entries in Table 1 indicates that the best upper bound was obtained from the 3-variable mechanism of Figure 13. Generally speaking, this model gives quite good upper bounds for tunnels with H/B ratios in the range 2 to 4, and may improve on the kinematic finite element results by up to 10 percent. Typically, however, the results from these two procedures are within a few percent of one another, with the 3-variable mechanism becoming increasingly inaccurate for increasing values of H/B .

CONCLUSIONS

The undrained stability of a square tunnel in a soil whose strength is permitted to vary linearly with depth has been studied. The application of two numerical schemes, which employ finite elements in conjunction with the classical limit theorems, has enabled tight bounds on the exact collapse pressures to be derived. The solutions presented are fully rigorous, since they satisfy all the conditions of the static and kinematic theorems.

ACKNOWLEDGEMENTS

The research reported in this paper is funded by a grant from the Australian Research Council. The Authors are thankful for this support and also wish to acknowledge the valuable comments made by Mr Peter Kleeman.

REFERENCES

1. Sloan S. W. (1988a). Lower bound limit analysis using finite elements and linear programming. *Int. J. Numer. Anal. Methods in Geomech.*, **12**, 61-67.
2. Sloan S. W. (1988b). A steepest edge active set algorithm for solving sparse linear programming problems. *Int. J. Numer. Methods Eng.*, **26**, 2671-2685.
3. Lysmer J. (1970). Limit analysis of plane problems in soil mechanics. *J. Soil Mech. Found. Div., ASCE*, **96**, SM4, 1131-1134.
4. Anderheggen E. and Knopf H. (1972). Finite element limit analysis using linear programming. *Int. J. Solids and Structures*, **8**, 1413-1431.

5. Pastor J. (1978). Limit analysis: numerical determination of complete statical solutions; application to the vertical cut. J. de Mécanique Appliquée (in French), 2, 167–196.
6. Bottero A., Negre R., Pastor J. and Turgeman S. (1980). Finite element method and limit analysis theory for soil mechanics problems. Comp. Meth. Appl. Mech. Eng., 22, 131–149.
7. Sloan S. W. (1989). Upper bound limit analysis using finite elements and linear programming. Int. J. Numer. Anal. Methods Geomech., 13, 263–282.

Received 22 December 1991; accepted 2 January 1992